

## Apparent cohesion effects on overtopping-induced fluvial dike breaching

ISMAIL RIFAI, Post-doctoral fellow, *Saint-Venant Hydraulics Laboratory, Chatou, France*

*Email: Rifaiismail@gmail.com (author for correspondence)*

KAMAL EL KADI ABDERREZZAK (IAHR Member), Expert Scientist, *National Laboratory for Hydraulics and Environment, Research & Development Division, Electricité de France, and Saint-Venant Laboratory for Hydraulics, Chatou, France*

*Email: kamal.El-kadi-Abderrezzak@edf.fr*

WILLI H. HAGER (IAHR Honorary Member), Emeritus Professor, *Laboratory of Hydraulics, Hydrology and Glaciology, Swiss Federal Institute of Technology, Zürich, Switzerland*

*Email: hager@vaw.baug.ethz.ch*

SEBASTIEN ERPICUM (IAHR Member), Assistant Professor, *Research Group Hydraulics in Environmental & Civil Engineering, Urban & Environmental Engineering, University of Liege, Liège, Belgium*

*Email: S.Erpicum@uliege.be*

PIERRE ARCHAMBEAU, Research Associate, *Research Group Hydraulics in Environmental & Civil Engineering, Urban & Environmental Engineering, University of Liege, Liège, Belgium*

*Email: Pierre.Archambeau@uliege.be*

DAMIEN VIOLEAU (IAHR Member), Senior Scientist, *National Laboratory for Hydraulics and Environment, Research & Development Division, Electricité de France, and Saint-Venant Laboratory for Hydraulics, Chatou, France*

*Email: Damien.Violeau@edf.fr*

MICHEL PIROTTON, Full Professor, *Research Group Hydraulics in Environmental & Civil Engineering, Urban & Environmental Engineering, University of Liege, Liège, Belgium*

*Email: Michel.Pirotton@uliege.be*

BENJAMIN DEWALS (IAHR Member), Professor, *Research Group Hydraulics in Environmental & Civil Engineering, Urban & Environmental Engineering, University of Liege, Liège, Belgium*

*Email: B.Dewals@uliege.be*

*Running Head: Apparent cohesion effects on dike breaching*

# Apparent cohesion effects on overtopping-induced fluvial dike breaching

## ABSTRACT

Flow overtopping can lead to the initiation of breaching and failure of fluvial dikes, causing severe inundations and damage in the protected areas. For flood risk management and prevention, the accurate estimate of flow discharge across the fluvial dike breach is paramount, requiring the precise understanding of the breach expansion. Laboratory experiments were conducted to analyse the effects of fine sand, inducing apparent cohesion in the dike material, on the breach development and outflow. Tests were conducted under controlled inflow discharge and dike material composed of either homogeneous non-cohesive coarse sand or heterogeneous fine sand/coarse sand mixtures. Based on the non-intrusive Laser Profilometry technique, high temporal and spatial resolution of the three-dimensional breach geometry evolution was measured, indicating a small effect of the fine material on the overall breach dynamics. A detailed analysis revealed, however, that fine sand induces less frequent slope collapses but larger sliding/failing lumps compared to homogenous non-cohesive coarse sand.

*Keywords:* Apparent cohesion; breaching; dike; laboratory studies; lump failure; overtopping flow.

## 1 Introduction

The construction of fluvial dikes (i.e. dykes, embankment levees) is typically followed by urban development in the protected floodplains. Floods subsequent to fluvial dike failure can therefore cause severe human and economic losses (Di Baldassarre et al., 2015). Flow overtopping can promote external erosion, leading to the initiation of dike breaching, potentially brutal failure and inundation of the protected areas (Foster et al., 2000; Jandora & Říha, 2008; Fry et al., 2012). To evaluate potential consequences of the induced floods, a thorough understanding of dike breaching mechanism is required.

Available knowledge on processes involved in dike failure relies generally on laboratory studies and numerical modelling (Rifai et al., 2018a; Onda et al., 2019), because monitoring of prototype dike breaching and failure events is hardly feasible. A number of studies have focused on *dams*, i.e. transversal/frontal obstacle to the flow (e.g. Coleman et al., 2002; Morris et al., 2007; Pickert et al., 2011; Schmocker & Hager 2012; Frank, 2016), but their results cannot be transferred to fluvial dikes because the flow in the breach near-field is highly influenced by the parallel flow to the dike (Michelazzo et al., 2015; Rifai et al., 2017; Rifai, 2018). The few studies on fluvial dikes deal with relevant issues such as: (i) breach development phases (Kakinuma et al., 2013; Rifai et al., 2017; Michelazzo et al., 2018), (ii) influence of riverbed and dike material (Islam, 2012; Kakinuma et al., 2013), (iii) deposition and erosion mechanisms in riverbed and floodplain resulting from the breach formation

(Islam, 2012; Kakinuma & Shimizu, 2014), and (iv) effects of main channel inflow and floodplain backwater on the breach dynamics (Michelazzo et al., 2018; Rifai et al., 2018a). Other key aspects relating to the fluvial dike composition still require investigation, because the dike material covers an extended range, from cohesive (e.g. Lower Rhine River, Lower Rhone River) to coarse sediments (e.g. Upper Rhone River, Missouri River).

This work is part of an ongoing research program aiming to improve the understanding of the physical processes involved in fluvial dike breaching due to flow overtopping. The experimental work investigates a broad range of main channel and floodplain configurations (Rifai et al., 2017; Rifai, 2018) as well as dike material. All experiments were monitored in detail, with time series of water levels in the main channel, time series of flow discharges in the main channel and across the breach, and high resolution 3-D reconstructions of the evolving dike geometry (Rifai et al., 2019). The dataset is open source and available online (Rifai et al. 2018b).

The present work aims to shed light on the effects of apparent cohesion, particularly on the slope failure dynamics during breach widening. Apparent cohesion encompasses both effects of effective cohesion and matric suction cohesion (Wood et al., 2001; Lu & Likos, 2006). Cohesion due to negative pore water pressure in unsaturated coarse material results from the attraction of water molecules in the interstitial space of the soil matrix (Ward & Robinson, 1990; Rinaldi & Casagli, 1999). It is responsible for the stability of nearly vertical breach side slopes or overhanging dike material blocks. Pickert et al.'s (2011) experiments on dam breaching highlighted the effects of finer material, inducing stronger apparent cohesion, sudden collapses of the breach side slopes, and thus sharper edged breach shapes. Assuming a gradual and continuous erosion process, applicable for dams and dikes composed of coarse material, becomes less valid for dikes composed of finer material. A tensile strength approach is necessary to approximate water-soil interactions. Works on fluvial dikes, such as those of Islam (2012) and Kakinuma et al. (2013), highlighted differences in the breaching dynamics according to the dike material composition. However, fine sediment inducing apparent cohesion was not investigated deeply. Laboratory studies remain scarce and no clear-cut conclusions are available so far.

This paper presents a series of fluvial dike breaching tests with different material compositions: homogenous coarse sand and bimodal material composed of coarse sand mixed with fine sand, in gradually increasing portions, inducing apparent cohesion. Section 1 outlines the experimental model and the monitoring systems. In section 2, the results are presented, from the overall breaching dynamics to detailed analysis of the breach expansion. Results are discussed in section 3, followed by concluding remarks in section 4.

## 2 Laboratory experiments

### 2.1 Laboratory setup

The experiments were conducted in the fluvial dike model at the National Laboratory of Hydraulics and Environment of the Research and Development (R&D) division of Electricité de France (EDF) (Fig. 1a). The experimental model consisted of a  $L_{mc} = 15.5$  m long and  $l_{mc} = 1.8$  m wide channel, with a  $L_d = 7$  m long side opening toward a  $1 \times 7$  m floodplain (Fig. 1b and c). The main channel and the floodplain were at the same level. A perforated plane located at the downstream end regulated the flow. This system with evenly distributed holes allowed for a quasi-uniform velocity distribution over the cross section.

The side opening was closed with a dike,  $h_d = 0.3$  m high, of trapezoidal shape with a  $l_{dc} = 0.1$  m wide crest. The inner and outer dike face slopes were  $S_i = S_o = 1:2$  (V:H); the bottom dike width was  $l_d = h_d / S_i + h_d / S_o + l_{dc} = 1.3$  m. To ensure dike stability against seepage, a drainage system was placed at the dike bottom (Fig. 1a and b). The drainage system consisted of a 4 cm-thick layer of coarse sand wrapped in a geotextile placed in a coarse grid. A 0.02 m deep and 0.1 m wide notch was cut at the dike crest at  $x = 2.5$  m to initiate flow overtopping at the same location for all experiments.

### 2.2 Dike composition

Different dike materials were tested, namely uniform coarse sand of median diameter  $d_{50} \approx 1$  mm (Material 1), and three heterogeneous compositions consisting of Material 1 mixed with fine sand (Material F) of  $d_{50} = 0.24$  mm. These mixtures were prepared according to three different volumetric fine sand ratios of 10% (Material F1), 20% (Material F2), and 30% (Material F3), respectively (Table 1). Due to water turbidity, consideration and compatibility with the breach geometry monitoring technique (cf. Section 2.4), the finer sediment portion was limited to 30%. A detailed laboratory characterization of all tested materials is given in Table 1, whereas Fig. 2 shows the corresponding grain size distributions. The wet coarse sand (Material 1) exhibits a very high friction angle because surface tension between the water and the grains tends to hold the grains in place (García, 2008).

### 2.3 Test program and test procedure

The effects of the main channel inflow discharge  $Q_i$  were extensively investigated by Rifai et al. (2017). Herein, the focus is on the effects of apparent cohesion. Table 2 presents the overall test program, where two inflow discharge series  $Q_i$  were tested, i.e. moderate ( $0.093 \text{ m}^3 \text{ s}^{-1}$  to  $0.096 \text{ m}^3 \text{ s}^{-1}$ ) and high ( $0.114 \text{ m}^3 \text{ s}^{-1}$  to  $0.125 \text{ m}^3 \text{ s}^{-1}$ ). The corresponding inlet initial Froude number *prior* to overtopping  $F_{i0} = [l_{mc} \times Q_i / (A_{mc}^3 \times g)]^{0.5}$  are 0.132 – 0.140 and

0.162 – 0.177, respectively, with  $A_{mc}$  the channel flow cross sectional area and  $g$  the gravity acceleration. Tests were conducted for four different dike compositions. The heterogeneous mixtures F1, F2, F3 were discarded after each test and not reused to avoid any effect of sediment sorting. The dike was placed by staking and compacting manually the material to avoid any structural defects. The manual compaction was deemed as constant compactive effort. A trapezoidal template was swiped along the longitudinal  $x$ -axis to shape the dike and remove excess material. The initial notch was then cut.

The perforated plane configuration (i.e. number of orifices and their arrangement) matched the test inflow discharge  $Q_i$  with the water level  $z_w$  in the main channel at the dike crest level (i.e.  $h_d = z_w = 0.3$  m). The main channel was therefore filled with gradually increasing inflow discharge up to  $Q_{i0} = 0.75 \times Q_i$ . This insured the filling of the channel just below the initial notch level to inspect the dike for any defects and to check the proper functioning of the drainage system. The inflow discharge was then increased to  $Q_i$ .

During dike breaching, the flow across the breach was discharged freely from the floodplain. The tests were stopped when the breach sides almost reached the concrete part of the side opening, close to the gauging point G2 (Fig. 1b).

#### 2.4 Measurements

Monitoring of water levels and flow discharges is detailed by Rifai et al. (2017, 2018a). Locations of the gauge stations G<sub>1</sub> to G<sub>6</sub> are shown in Fig. 1b. The breach discharge  $Q_b$  is deduced from the mass balance adapted to the control volume of the main channel (Fig. 1b):

$$Q_b(t) = Q_i(t) - Q_o(t) - Q_d(t) - (A_{G1} + A_{G2} + A_{G3}) \times dz_w/dt \quad (1)$$

with  $t$  as time;  $z_w = (A_{G1}z_{G1} + A_{G2}z_{G2} + A_{G3}z_{G3}) / (A_{G1} + A_{G2} + A_{G3})$  as the weighted average of water levels  $z_{G1}$ ,  $z_{G2}$ , and  $z_{G3}$  at G<sub>1</sub>, G<sub>2</sub>, and G<sub>3</sub> gauge stations, respectively, with  $A_{G1}$ ,  $A_{G2}$ , and  $A_{G3}$  as main channel surface areas associated with G<sub>1</sub>, G<sub>2</sub>, and G<sub>3</sub>, respectively (Fig. 1b).  $Q_d$  is the drainage discharge and  $Q_o$  is the main channel outflow discharge, both deduced *via* prismatic routing at G<sub>4</sub> and G<sub>5</sub>.

The 3-D breach evolution was monitored by a non-intrusive Profilometry technique consisting of a sweeping laser plan (emitted by a laser line projector Z-Laser Z30M18S3-F-640-LP75) by two projectors fixed to an automated sliding rail system over the dike (Rifai et al., 2016; 2017; 2018a). The recording was performed by a digital camera set on 1920×1080 pixels resolution. The 3-D reconstruction algorithm of the dike geometry includes optical distortion and refraction correction modules for submerged dike portions. Further details on the breach geometry reconstruction are given by Rifai et al. (2016). Repeatability of experiments and accuracy of measurements are extensively discussed in Rifai et al. (2019).

### 3 Results

#### 3.1 Overall breaching dynamics

The breaching process remained qualitatively identical for all tests. For the sake of brevity, we only describe Test 1a (Fig. 3). The breaching stages agree with those proposed by Rifai et al. (2017): Stage 0 with gradual and slow initiation of flow overtopping inducing dike erosion (Fig. 3,  $t \approx 0 - 20$  s), Stage 1 with fast breach deepening and widening along with highly transient flow (Fig. 3,  $t \approx 33 - 160$  s), and Stage 2 with quasi-stabilization of the flow (i.e. almost constant breach outflow discharge) and sustained breach expansion (Fig. 3,  $t > 390$  s). The transition between Stage 1 and Stage 2 occurs at approximately three times a timescale defined as the ratio between the main channel volume and the inflow discharge  $Q_i$ .

#### 3.2 Breach expansion

Figure 4 shows the temporal evolutions of the breach width  $w_b$  and breach invert depth  $z_b$  for tests with different inflow discharges and dike materials. A data scatter was noted for the breach widening plots for tests with the same inflow discharge intensity (Fig. 4a), but no trend was deduced according to the dike composition. Even a focus on the first 500 s (Fig. 4b and c) does not highlight a clear effect of the material on the breach widening. Tests conducted with homogeneous coarse sand (Material 1) (black bold line in Fig. 4b and black dash-dotted line in Fig. 4c) display a relatively faster widening, but this effect appears to be due to the slightly higher inflow discharge  $Q_i$  in Tests 1a and 1b. The breach depth evolution (Fig. 4d to f) shows a moderate effect of dike composition. Breach deepening was faster for tests with finer material, especially under higher inflow discharges (Fig. 4f).

#### 3.3 Breach discharge and water levels

Figure 5 shows the evolution of the breach discharge  $Q_b$  and the main channel water levels  $z_w$  for different fine sand ratios. No significant effect of the finer material is noted. During Stage 2, differences in the small breach discharges are observed. These are attributed to variations in the inflow discharge slightly differing in-between the tests for the same “inflow discharge level” (moderate or high), and to differences in the drainage discharge  $Q_d$  which was around 0.008, 0.007, 0.004, and 0.002  $\text{m}^3 \text{s}^{-1}$  for tests with Mat. 1, F1, F2, and F3, respectively. The drainage discharge decreased as finer material was added to the mixture, clogging the coarser sediment matrix, and thus reducing the dike material permeability. The drainage discharge was measured prior to overtopping when the channel water level was almost at the notch level. A setback of the seepage line, due to the addition of a finer portion into the sediment mixture, was also noted from small inspection holes on the dike floodplain bank at test start.

Zooms covering Stages 0 and 1 on  $Q_b$  time series (Fig. 5b and c) evidence that tests with a higher fine sediment portion have a faster breach discharge increase and a trend to develop a peak discharge (Red dash-dot and red solid lines in Fig. 5b and c). Differences in  $Q_b$  during Stage 1 are consistent with the differences in the breach deepening dynamics (cf. Section 3.2), as for equivalent channel water level, deeper breaches convey higher breach outflow.

Channel water levels  $z_w$  do not show significant differences overall (Fig. 5d). However, a focus on Stages 0 and 1 shows a ranking of the water level time series according to the ratio of finer material. A higher fine sediment portion induces a faster decrease in the water level (Fig. 5e and f), in agreement with the breach discharge values as a faster increase in  $Q_b$  induces a faster emptying of the main channel.

## 4 Discussion of results

### 4.1 Breach shape

Overall, the time series of breach discharge, widening and deepening do not fully evidence the effects of sediment grading on the breaching process. Therefore, a close investigation of the breach shape for the tested dike compositions was performed. Figure 6 shows images from the recorded footage of tests under high inflow intensity, i.e. Tests 1b, 2b, 3b, and 4b, during the first 60 s. As the surface erosion occurs ( $t \approx 35$  s), differences in the resulting breach channel slopes are visible. For instance, milder slopes form for homogeneous sand, whereas steeper slopes with a hydraulic jump at the dike toe form for Material F3 (pink circled detail in Fig. 6 at  $t = 35$  s). At  $t = 45$  s, the breach hourglass shape remains narrower at the downstream dike face for tests with higher fine sand portion (blue circled detail in Fig. 6 at  $t = 45$  s). Figure 6 shows that at  $t = 55$  s, the breach crosswise slope is steeper for tests with a higher finer portion. In addition, reflections on the flow surface by the same light spot, suggest a different free flow surface curvature, due to the breach cross section shape (green circled detail in Fig. 6 at  $t = 55$  s).

Figure 7 illustrates the evolution of the breach cross-sectional profile, highlighting the effect of finer material on the breach dynamics. For Test 1a, i.e. homogeneous sand and medium inflow intensity, a radial erosion of the dike downstream face is noted (Fig. 7a) with the collapse of the dike downstream face around a pivot point located close to the dike downstream toe. Sediment deposition was also noted at the dike toe. For higher flow intensity (Tests 1b, Fig. 7b), the breach widening mainly occurred downward in the main channel flow direction, and the lowest breach point quickly shifted toward downstream. Therefore, the breach cross-section at the initial notch location does not allow observing the breach lowest

point evolution. Tests with finer sediment portion involve a gradually changing breach cross-section behaviour (Fig. 7c-h).

The breach expansion is mainly bedload transport driven. The setback of the pivot point can be explained by the sediment size. For homogenous sand (i.e. Mat. 1,  $d_{50} = 1$  mm), the material eroded from the dike crest was deposited at the dike toe, inducing a gradual reduction of the breach downstream slope. However, for bimodal sand (e.g. Mat. F3,  $d_{50} = 0.91$  mm) the material eroded from the dike crest was easily washed away causing a parallel erosion of the dike downstream face as well as a gradual setback of the pivot point. Sediment deposition at the downstream toe was less important for tests with finer sediment portion. Figure 7g shows an undulation downstream of the pivot point due to the local hydraulic jump at this location (pink circled detail in Fig. 6 at  $t = 35$  s). This observation agrees with similar experiments on dams (Schmocker & Hager, 2012).

It should be noted that the slight decrease in the median diameter  $d_{50}$  might not be the only parameter increasing the bedload transport. The addition of a finer non-cohesive sediments might increase bedload due to the hiding-exposure effects. Indeed, the critical shear stress required to mobilise the coarse sediments decreases due to the exposure effect, whereas hiding leads to a decrease in the threshold motion of the finer grains (McCarron et al. 2019).

The longitudinal breach profiles illustrate the effect of finer sediment portion on the lateral breach expansion and shape (Fig. 8). Tests with uniform coarse sand yield shallower breaches. For Test 1b (Fig. 8b), the breach rapidly shifted in the downstream direction. Increase in the finer portion induced narrower longitudinal breaches during the first 60 s. Overall, the results agree with other experiments on the effect of apparent cohesion in terms of alteration of the breach cross-sectional and longitudinal profiles, a shift to parallel rather than radial erosion, delay of the formation of the pivot point, and setback of the pivot point closer to the crest (Coleman et al., 2002; Pickert et al., 2011; Schmocker & Hager, 2012; van Emelen et al., 2015).

#### 4.2 *Lump failure*

Tests conducted with a finer sediment portion showed noticeable differences in the breach shape and in the evolution of the breach cross-sectional profile, while no particular trend was noted on the breach widening during Stage 2 nor on the process duration (Fig. 4a and d). Nevertheless, differences in the process, such as slope failure during Stage 2, were visually observed. Additional post-processing of the video recordings was therefore conducted. It consisted of extracting 3-D reconstructions of the longitudinal dike profile at the crest level at a higher time resolution, resulting in 500 to 1000 longitudinal profiles per test, and thus refined breach widening time series. Figure 9, which is a higher time resolution version of

Fig. 4a, shows that the breach widening during Stage 2 (around  $t > 300$  s) occurred by slope collapses and slumping of the dike downstream side. This is evidenced by the *stair*-like shape of the plots: successive sudden increases in breach width  $w_b$ , followed by a “plateau”.

The high resolution breach width time series were processed to isolate individual slope and lump failure events (Fig. 9, circled detail). Only Stage 2 was accounted for, because slope failures occurred during this stage, whereas during Stage 0 and 1 the breach expansion was more gradual. Due to the scattering of the data, the detection of the breach widening “episodes” was performed manually. The processing allowed for the assessment of the breach failure events in terms of typical times  $dt$  between successive slope failures and the amount of material collapsed at each failure event, *via* the failing lump widths  $dw_b$  (Fig. 9, circled detail). Figure 10 shows the effects of dike material on the breach expansion dynamics during Stage 2. For higher fine material ratios, times between slope failure events  $dt$  increase (Fig. 10a and d). Conversely, the size of failed lumps and the breach width differences between two slope failure events increase with the fine sand ratio (Fig. 10b and e). Overall, the temporal increase between two successive slope failure events tends to be compensated by the size of the failed lumps. Therefore, the mean breach widening rate remains substantially the same for tests with the same inflow discharge and different dike compositions (Fig. 10c and f). This latter aspect agrees with width time series, during Stage 2, plotted in Figs. 4 and 9, which are relatively close regardless of the dike composition.

Figure 10 also shows that differences in-between tests with different inflow discharges are higher for the time step between successive failure events  $dt$  than for the size of failing lumps (Fig. 10a, b, d, and e). This suggests that, for the tested ranges of material and inflow discharges, the dike composition influences the size of failing lumps sizes and, thus, the time  $dt$  necessary for the failed material to be eroded, whereas hydraulic loads mainly affect the erosion rate of the failed lumps but not their size.

The range of tested dike compositions remains in the domain of non-cohesive material. However, effects of apparent cohesion, as defined by Terzaghi et al. (1996) and Rinaldi & Casagli (1999), were noted: cohesion occurs due to capillarity pressure, but completely disappears once the material is submerged. This particular aspect was noted during the experiments, as failing clustered lumps quickly “dissolve” once submerged, losing their structural integrity once saturated (Fig. 11). This suggests that changes in  $dt$  between two slope failure events, i.e. the time necessary to erode all failed material, are mainly due to the amount of material failed and to be eroded, though the erosion rate remains substantially the same. Effects of lump composition, once failed, seems to remain negligible at this stage. Thus including a portion of fine sediments in the dike material results in a double effect on the breach widening dynamics during Stage 2: less frequent slope failure events; but larger

collapsing volumes. Surprisingly, these two effects tend to cancel each other, resulting in virtually no influence of the fine sediment portion on the breach widening rate.

A comparison of Figs. 10c and 10f shows that, in the tested range of dike material and inflow discharge  $Q_i$ , the latter has a stronger effect on the breach widening rate. Indeed, the regression lines are almost horizontal, but with a strong offset between tests conducted with different  $Q_i$ . Moreover, during Stage 2, the breach widens mainly in the channel flow direction, with the expansion caused by breach-through-flow induced erosion (Rifai et al., 2017). These two aspects contrast with the fact that effects of the inflow discharge and channel flow velocity are commonly disregarded in existing parametric or numerical models.

## 5 Conclusions

An experimental campaign was conducted to investigate the effects of apparent cohesion due to fine sand on the breaching of fluvial dikes induced by flow overtopping. Homogenous coarse sand, and three sediment mixtures composed of fine sand and coarse sand were tested as dike materials. The instrumentation of the experimental setup allowed for monitoring water levels, flow discharges, and full high time-resolved 3-D reconstructions of the dike geometry.

The experimental observations highlight three stages in the breaching process: gradual start of flow overtopping and slow initiation of dike surface erosion (Stage 0), fast breach deepening and widening with transient flows (Stage 1), and flow quasi-stabilization with sustained breach widening (Stage 2). During Stage 0, the presence of finer material in the dike composition significantly reduces the drainage discharge and induces a setback of the seepage line. Regarding the breach evolution and breach flow discharge, no strong effects were observed, particularly during Stage 2. During Stages 0 and 1, the breach cross-sectional profiles reveal a parallel rather than a radial erosion of the downstream dike face in the presence of fine sand, as observed for coarse sand. Moreover, the pivot point migrates upstream for heterogeneous dike composition, and the breach channel is also more incised. Consequently, the breach discharge increases slightly faster. During Stage 2, the breach widening rates are globally similar. Yet, based on a detailed analysis, the dynamics of slope failure is affected by the dike composition, with less frequent side collapses and bigger sliding/failing lumps for higher fine material portion.

These experiments are limited in terms of tested dike compositions and inflow discharges. However, they bring an interesting insight on the effects of adding fine non-cohesive sediments in a coarser non-cohesive dike material. This aspect can be of crucial interest if using a finer non-cohesive material is considered as an option to reduce the drainage capacity of the dike material, or if the available material for dike construction is a bimodal non-cohesive mixture. In addition, the apparent cohesion effects observed on the

breach expansion and stability shed light on the shortcomings of available and routinely used numerical models, in which slope and lump failures are often modeled based on a simple stability criterion using a dry and/or saturated friction angle of the dike material. They do not fully include the mechanisms involved in an unsaturated material, as observed during dike breaching, where matric suction cohesion induces nearly vertical slopes. The numerical modelling of Volz et al. (2017) tackles this issue by including seepage flow across the dike. Further refinement and validation of these tools is still called for to pave the way for improvements of engineering appraisal-level numerical models for predicting the breaching of dikes and associated floods.

### **Acknowledgements**

The authors acknowledge the support of the *Fonds Spéciaux de la Recherche* (FSR) of the University of Liège, Belgium.

### **Funding**

This work was partially funded by the *Association Nationale de Recherche et de la Technologie* (ANRT) [CIFRE #2015/0015], the European Fund FEDER (*Programme Opérationnel Interrégional Rhône-Saône* 2014-2020) and EDF.

### **Notation**

$A_{Gi}$  = flow surface area associated to gauge  $G_i$  ( $m^2$ )

$d_{50}$  = median diameter of material (m)

$F_{i0}$  = Froude number in main channel prior to overtopping (-)

$h_d$  = dike height (m)

$l_{dc}$  = dike crest width (m)

$L_d$  = dike length (m)

$l_d$  = dike width (m)

$l_{mc}$  = main channel width (m)

$L_{mc}$  = main channel length (m)

$p$  = porosity (-)

$Q_b$  = breach discharge ( $m^3 s^{-1}$ )

$Q_d$  = drainage discharge ( $m^3 s^{-1}$ )

$Q_i$  = test inflow discharge ( $m^3 s^{-1}$ )

$Q_{i0}$  = channel filling inflow discharge ( $m^3 s^{-1}$ )

$Q_o$  = main channel outflow discharge ( $m^3 s^{-1}$ )

$S_i, S_o$  = dike side slopes, i.e. channel side and floodplain side, respectively (-)

$t$  = time (s)  
 $x$  = coordinate on  $x$  axis (m)  
 $y$  = coordinate on  $y$  axis (m)  
 $z$  = coordinate on  $z$  axis (m)  
 $z_b$  = breach invert elevation (m)  
 $z_{Gi}$  = water level at gauging station  $G_i$  (m)  
 $z_w$  = averaged water level in main channel (m)  
 $\rho_b$  = sediment bulk density ( $\text{kg m}^{-3}$ )  
 $\rho_s$  = sediment density ( $\text{kg m}^{-3}$ )  
 $\varphi$  = Friction angle/angle of repose dry ( $^\circ$ )  
 $\varphi_w$  = Friction angle/angle of repose wet ( $^\circ$ )

## References

- Coleman, S. E., Andrews, D. P., & Webby, M. G. (2002). Overtopping breaching of noncohesive homogenous embankments. *Journal of Hydraulic Engineering*, 128(9), 829–838.
- Di Baldassare, G., Viglione, A., Carr, G., Kuil, L., Yan, K., Brandimarte, L., & Blöschl, G. (2015). Debates-perspectives on socio-hydrology: Capturing feedbacks between physical and social processes. *Water Resources Research*, 51(6), 4770–4781.
- Foster, M., Fell, R., & Spannagle, M. (2000). The statistics of embankment dam failures and accidents. *Canadian Geotechnical Journal*, 37(5), 1000–1024.
- Frank, P.-J. (2016). *Hydraulics of spatial dike breach* (Doctoral dissertation). ETH Zürich, Switzerland.
- Fry, J.-J., Vogel, A., Royet, P., & Courivaud, J.-R. (2012, August). Dam failures by erosion: Lessons from ERINOH databases. In Fry, J.-J., & C. Chevalier (Eds.), *ICSE 2012. Proceedings of the 6th International Conference on Scour and Erosion*. Paris, France: SHF
- García, M. H. (2008). Chapter 2: Sediment Transport and Morphodynamics. In M. H. García (Ed.), *Sedimentation Engineering: Processes, Measurements, Modeling, and Practice* (pp. 21–163). Reston, VA: ASCE.
- Islam, S. (2012). *Study on levee breach and successive disasters in low-land through numerical and experimental approaches* (Doctoral dissertation). Nagoya University, Japan.
- Jandora, J., & Ríha, J. (2008). *The failure of embankment dams due to overtopping*. Brno, Czech Republic: Vutium.

- Kakinuma, T., & Shimizu, Y. (2014). Large-scale experiment and numerical modeling of a riverine levee breach. *Journal of Hydraulic Engineering*, *140*(9), 1–9.
- Kakinuma, T., Tobita, D., Yokoyama, H., & Takeda, A. (2013, September). Levee breach observation at Chiyoda experimental flume. In S. Fukuoaka, H. Nakagawa, T. Sumi, & H. Zhang (Eds.), *ISRS 2013. Proceedings of the 12th International Symposium on River Sedimentation* (pp. 1013–1020). Kyoto, Japan: CRS press.
- Lu, N., & Likos, J. (2006). Suction stress characteristic curve for unsaturated soil. *Journal of Geotechnical and Geoenvironmental Engineering*, *132*(2), 131–142.
- McCarron, C. J., van Landeghem, K. J. J., Baas, J. H., Amoudry, L. O., & Malarkey, J. (2019). The hiding-exposure effect revisited: A method to calculate the mobility of bimodal sediment mixtures. *Marine Geology*, *410*, 22–31.
- Morris, M., Hassan, M., & Vaskinn, K. (2007). Breach formation: Field test and laboratory experiments. *Journal of Hydraulic Research*, *45*(sup1), 9–17.
- Michelazzo, G., Oumeraci, H., & Paris, E. (2015). Laboratory study on 3D flow structures induced by zero-height side weir and implications for 1D modeling. *Journal of Hydraulic Engineering*, *141*(10), 04015023.
- Michelazzo, G., Oumeraci, H., & Paris, E. (2018). New hypothesis for the final equilibrium stage of a river levee breach due to overflow. *Water Resources Research*, *54*(7), 4277–4293.
- Onda, S., Hosoda, T., Jaćimović, N. M., & Kimura, I. (2019). Numerical modelling of simultaneous overtopping and seepage flows with application to dike breaching. *Journal of Hydraulic Research*, *57*(1), 13–25.
- Pickert, G., Weitbrecht, V., & Bieberstein, A. (2011). Breaching of overtopped river embankments controlled by apparent cohesion. *Journal of Hydraulic Research*, *49*(2), 143–156.
- Rifai, I., Erpicum, S., Archambeau, P., Violeau, D., Piroton, M., El Kadi Abderrezzak, K., & Dewals, B. (2016, September). Monitoring topography of laboratory fluvial dike models subjected to breaching based on a laser profilometry technique. In S. Wieprecht, S. Haun, K. Weber, M. Noack, & K. Terheiden (Eds.), *ISRS 2016. Proceedings of the 13th International Symposium on River Sedimentation* (pp. 380–386). Stuttgart, Germany: CRS Press.
- Rifai, I., Erpicum, S., Archambeau, P., Violeau, D., Piroton, M., El Kadi Abderrezzak, K., & Dewals, B. (2017). Overtopping induced failure of noncohesive, homogeneous fluvial dikes. *Water Resources Research*, *53*(4), 3373–3386.
- Rifai, I. (2018). *Overtopping induced fluvial dike failure* (Doctoral dissertation). University Paris-Est, France, and University of Liège, Belgium.

- Rifai, I., El kadi Abderrezzak, K., Erpicum, S., Archambeau, P., Violeau, D., Piroton, M., & Dewals, B. (2018a). Floodplain backwater effect on overtopping induced fluvial dike failure. *Water Resources Research*, 54(11), 9060–9073.
- Rifai, I., El kadi Abderrezzak, K., Erpicum, S., Archambeau, P., Violeau, D., Piroton, M., & Dewals, B. J. (2018b). Accompanying dataset for: “Flow and detailed 3D morphodynamic data from laboratory experiments of fluvial dike breaching” *Zenodo*, <https://doi.org/10.5281/zenodo.1477843>.
- Rifai, I., El kadi Abderrezzak, K., Erpicum, S., Archambeau, P., Violeau, D., Piroton, M., & Dewals, B. (2019). Flow and detailed 3D morphodynamic data from laboratory experiments of fluvial dike breaching. *Scientific Data*, 6(1), 53.
- Rinaldi, M., & Casagli, N., (1999). Stability of streambanks formed in partially saturated soils and effects of negative pore water pressures: The Sieve River (Italy). *Geomorphology*, 26(4), 253–277.
- Schmocker, L., & Hager, W. H. (2012). Plane dike breaching due to overtopping: Effects of sediment, dike height and discharge. *Journal of Hydraulic Research*, 50(6), 576–586.
- Schmocker, L., Frank, P.-J., & Hager, W. H. (2014). Overtopping dike-breach: Effect of grain size distribution. *Journal of Hydraulic Research*, 52(4), 559–564.
- Terzaghi, K., Peck, R. B., & Mesri, G. (1996). *Soil mechanics in engineering practice*. Chichester: John Wiley & Sons.
- van Emelen, S., Soares-Fraza, S., & Zech, Y. (2015, 28 June–3 July). Breaching of small-scale sand embankments by overtopping. In A. Mynett (Ed.), *IAHR 2015. Proceeding of the 36<sup>th</sup> IAHR World Congress*. The Hague, The Netherlands: IAHR.
- Volz, C., Frank, P.-J., Vetsch, D. F., Hager, W. H., & Boes, R. M. (2017). Numerical embankment breach modelling including seepage flow effects. *Journal of Hydraulic Research*, 55(4), 480–490.
- Ward, R., & Robinson, M. (1967). *Principles of hydrology*. New York, NY: McGraw-Hill
- Wood, A. L., Simon, A., Downs, P., & Thorne, C. R. (2001). Bank-toe processes in incised channels: The role of apparent cohesion in the entrainment of failed bank materials. *Hydrological Processes*, 15(1), 39–61.

## **List of tables**

Table 1. Properties of material used for dike breaching experiments

Table 2. Overall test program

## List of figures

Figure 1 (a) View of experimental model, (b) plan sketch, and (c) side view of drainage system (profile A-A), with  $Q_i$  as inflow discharge,  $Q_b$  as breach discharge,  $Q_d$  as drainage discharge, and  $Q_o$  as main channel outflow discharge. The notch is located at  $x = 2.5$  m. The regulating system at downstream end is a perforated plate

Figure 2 Grain size distributions for Material F (fine sand), Material 1 (coarse sand), and three mixed grain size distributions F1, F2 and F3

Figure 3 3-D Reconstruction of breach evolution during Test 1a

Figure 4 (a) Breach width and (d) depth time series. (b) and (c) are a zoom on the first 500 s of (a) for moderate and high inflow discharges, respectively. (e) and (f) are a zoom on the first 500 s of (d) for moderate and high inflow discharges, respectively

Figure 5 (a) Breach discharge and (d) channel water level time series. (b) and (c) are zooms on the first 500 s of the breach discharge time series for moderate and high inflow discharge tests, respectively. (e) and (f) are zooms on the first 500 s of water level time series for moderate and high inflow discharge tests

Figure 6 Breach formation during the first 60 s for different dike compositions

Figure 7 Breach cross-section at approximately the initial notch level during the first 100 s; the time between each two profiles is approximately 4 s.  $\otimes$  location of *pivot point* (Schmocker & Hager, 2012)

Figure 8 Longitudinal breach profile at crest level during first 60 s; the time between each two profiles is approximately 4 s. The axis of initial notch is located at  $x = 2.55$  m

Figure 9 Evolution of breach width at crest level deduced from the high temporal resolution reconstructions of the breach profiles. The circled detail indicates how the failing lump widths  $dw_b$  and times between two lumps failure episodes  $dt$  are defined

Figure 10 Whiskers plots of: (a) and (d) time  $dt$  between two successive slope failures, (b) and (e) width  $dw_b$  of failing lumps, and (e) and (f) breach widening speed during Stage 2. The red horizontal line is the median, and the box lower and upper limits correspond to the 25<sup>th</sup> and 75<sup>th</sup> percentiles, respectively. The whiskers extend to the most extreme data points not considered outliers and outliers are plotted individually using the red + symbol. The subplots

(a) to (c) relate to tests with moderate inflow, (d) to (f) to tests with high inflow. The green and purple lines are linear regressions of the median  $dt$ ,  $dw_b$ , and  $dw_b/dt$  values for tests with different material compositions

Figure 11 Test 3b - Slope collapse and wash out of failed material by breach outflow

Table 1. Properties of material used for dike breaching experiments

	Material F (fine sand)	Material 1 (coarse sand)	Material F1	Material F2	Material F3
Median diameter $d_{50}$ (mm)	0.24	1.03	0.98	0.96	0.91
Volumetric ratio of fine sand (%)	100	0	10	20	30
Density $\rho_s$ (kg m <sup>-3</sup> )	2485	2470	2478	2503	2510
Bulk density $\rho_b$ (kg m <sup>-3</sup> )	1540	1556	1710	1877	1883
Porosity $p$ (-)	0.38	0.37	0.31	0.25	0.25
Friction angle dry $\varphi$ (°)	28-30	28	-	30	-
Friction angle wet $\varphi_w$ (°)	-	55	-	-	-
Tilt angle (°)	32	30	-	29	-

Table 2. Overall test program

Test-ID	Test-ID in Rifai <i>et al.</i> (2019)	Dike composition	$Q_i$ (m <sup>3</sup> s <sup>-1</sup> )	Inlet initial Froude number $F_{i0}$	Inflow intensity
1a	38	Material 1 (uniform coarse sand)	0.099	0.140	Moderate
2a	46	Material F1	0.096	0.137	
3a	48	Material F2	0.093	0.132	
4a	50	Material F3	0.095	0.134	
1b	39	Material 1 (uniform coarse sand)	0.125	0.177	High
2b	47	Material F1	0.114	0.162	
3b	49	Material F2	0.114	0.162	
4b	51	Material F3	0.115	0.163	

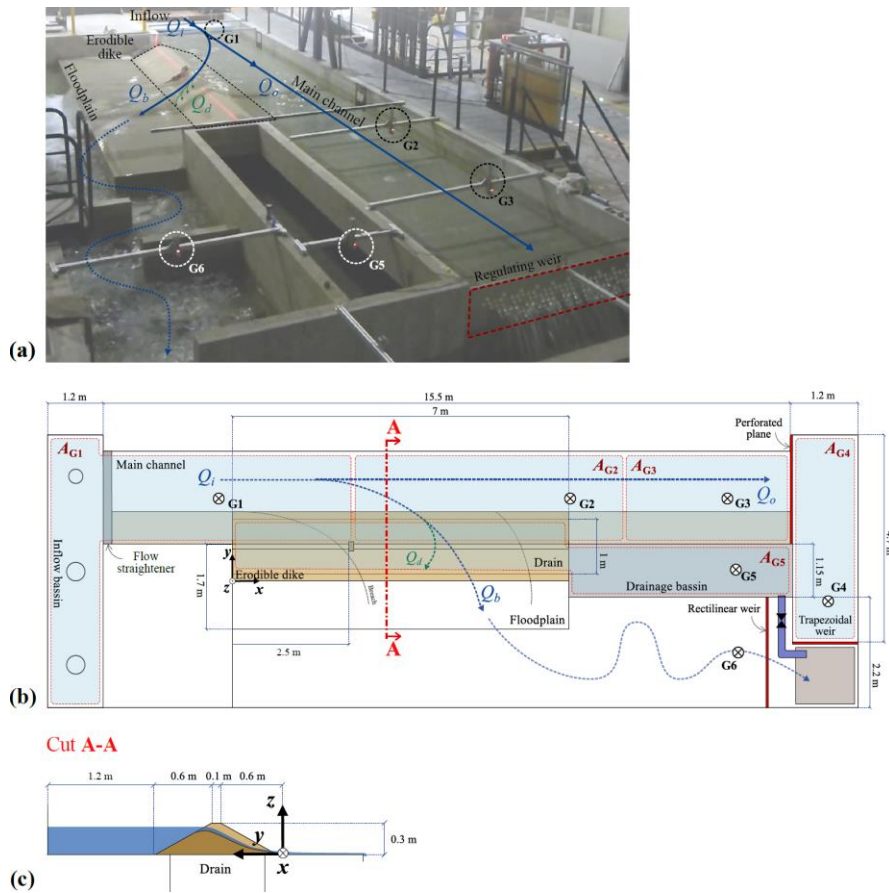


Figure 1 (a) View of experimental model, (b) plan sketch, and (c) side view of drainage system (profile A-A), with  $Q_i$  as inflow discharge,  $Q_b$  as breach discharge,  $Q_d$  as drainage discharge, and  $Q_o$  as main channel outflow discharge. The notch is located at  $x = 2.5$  m. The regulating system at downstream end is a perforated plate

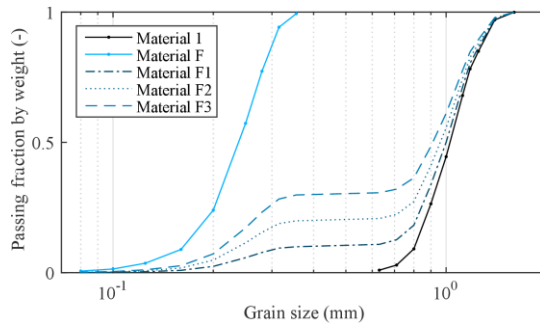


Figure 2 Grain size distributions for Material F (fine sand), Material 1 (coarse sand), and three mixed grain size distributions F1, F2 and F3

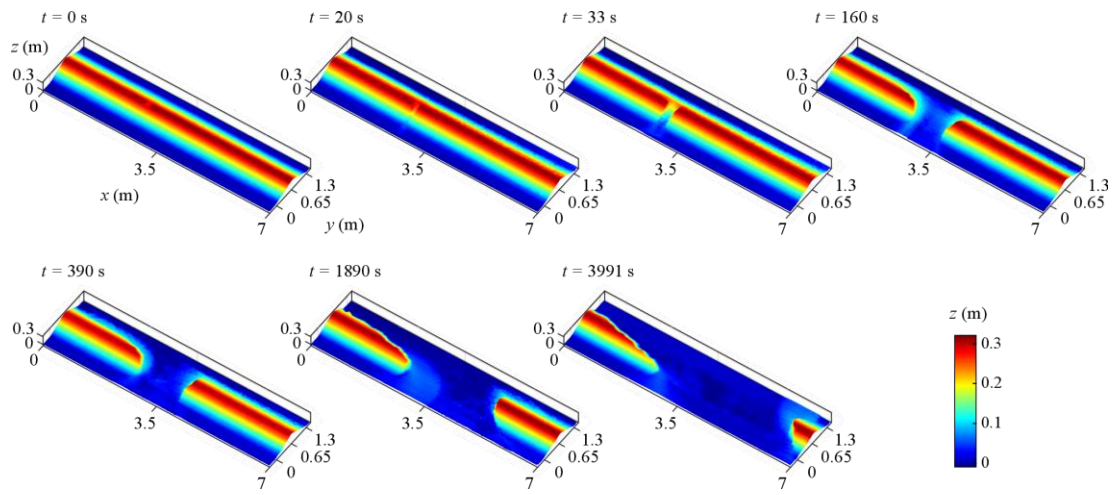


Figure 3 3-D Reconstruction of breach evolution during Test 1a

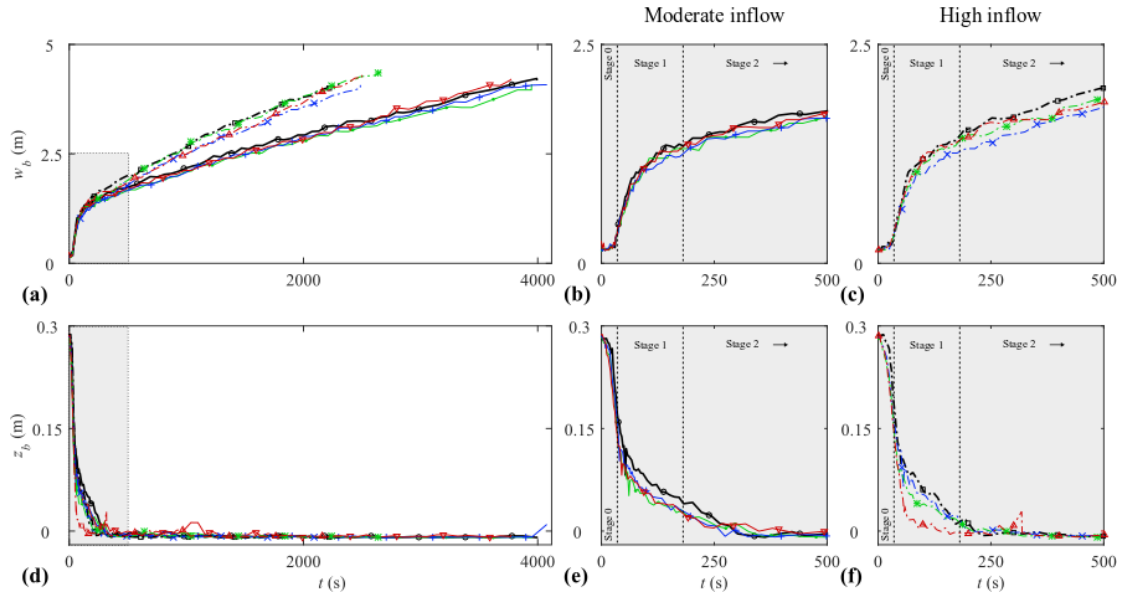
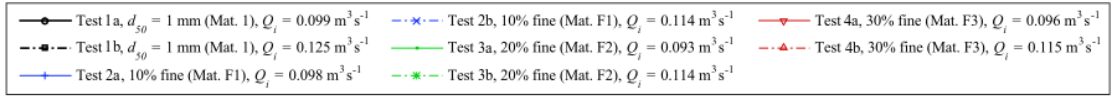


Figure 4 (a) Breach width and (d) depth time series. (b) and (c) are a zoom on the first 500 s of (a) for moderate and high inflow discharges, respectively. (e) and (f) are a zoom on the first 500 s of (d) for moderate and high inflow discharges, respectively

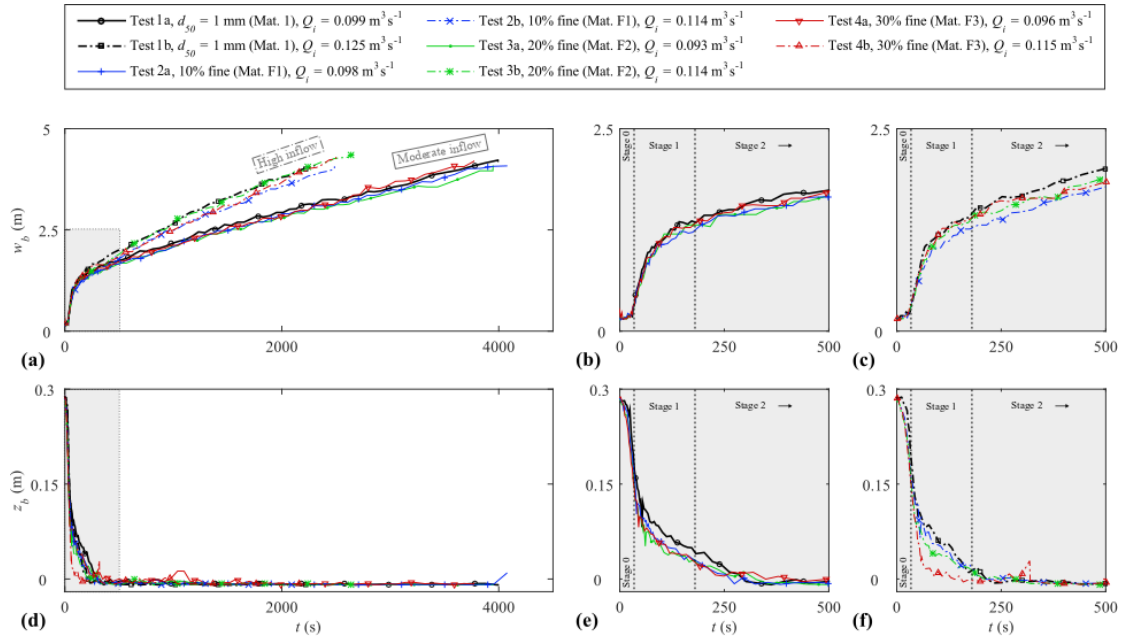


Figure 5 (a) Breach discharge and (d) channel water level time series. (b) and (c) are zooms on the first 500 s of the breach discharge time series for moderate and high inflow discharge tests, respectively. (e) and (f) are zooms on the first 500 s of water level time series for moderate and high inflow discharge tests

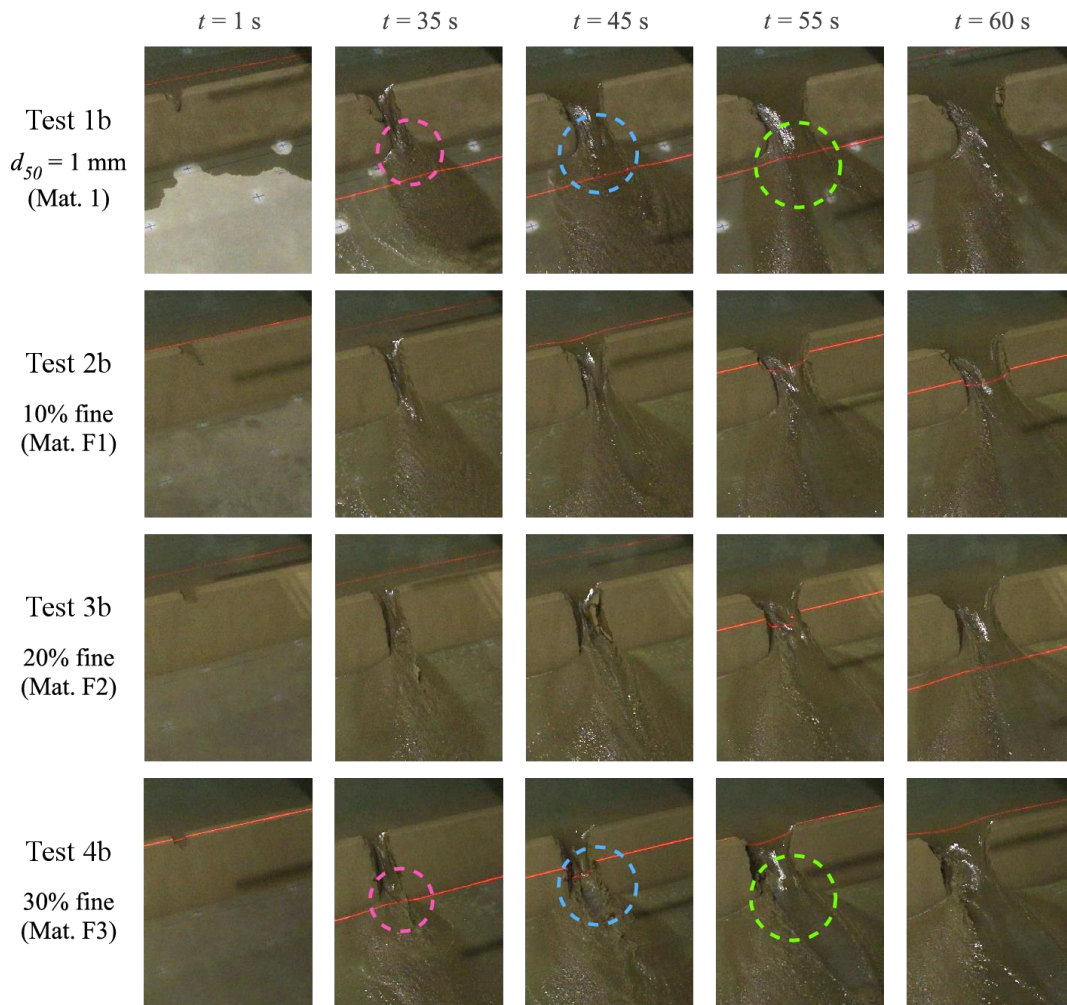


Figure 6 Breach formation during the first 60 s for different dike compositions

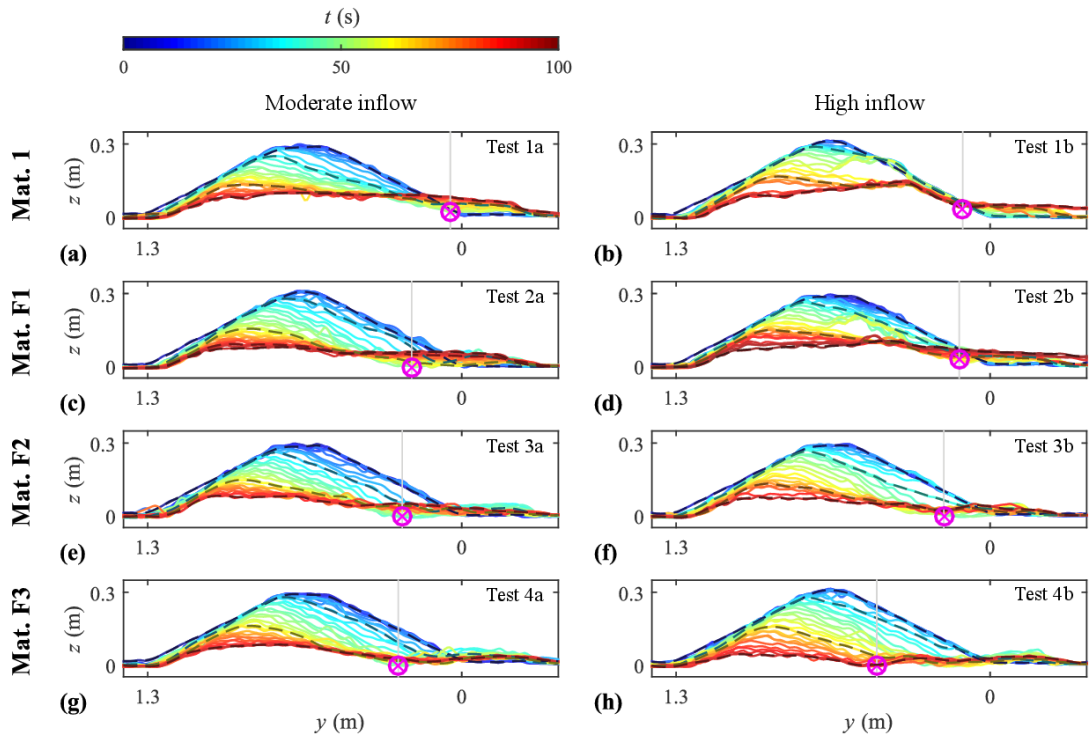


Figure 7 Breach cross-section at approximately the initial notch level during the first 100 s; the time between each two profiles is approximately 4 s.  $\otimes$  location of *pivot point* (Schmocker & Hager, 2012)

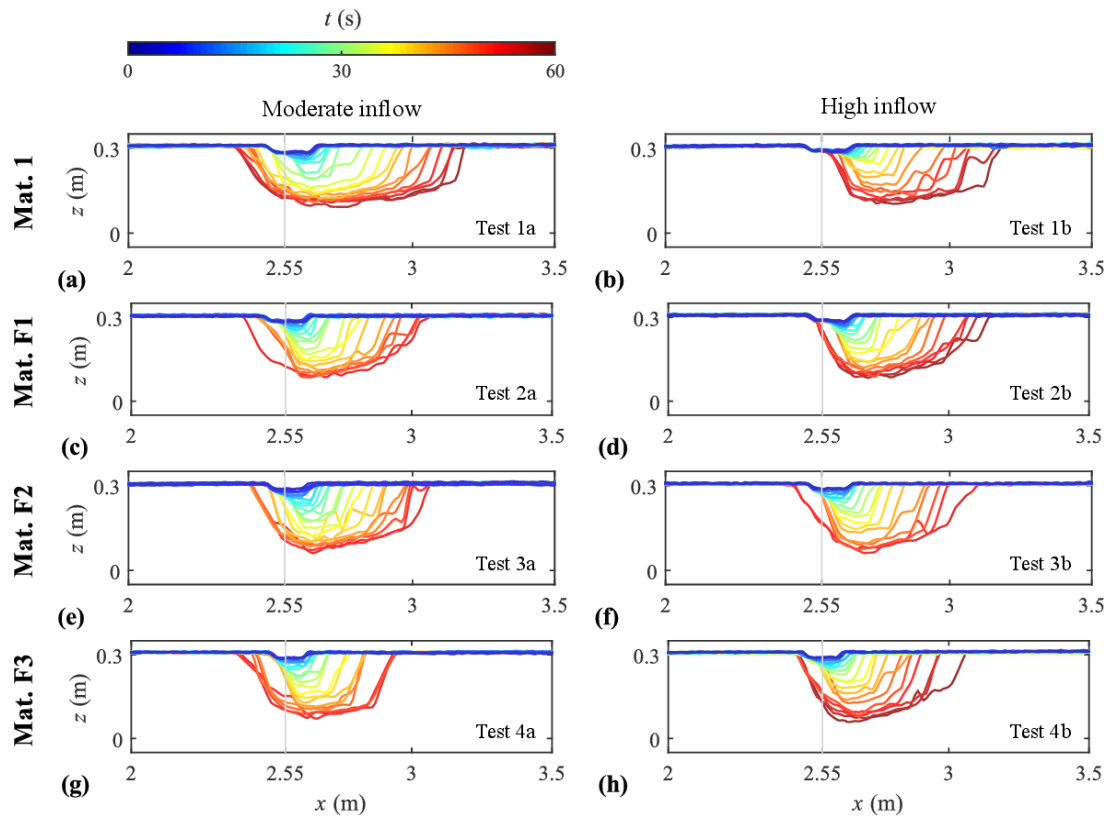


Figure 8 Longitudinal breach profile at crest level during first 60 s; the time between each two profiles is approximately 4 s. The axis of initial notch is located at  $x = 2.55$  m

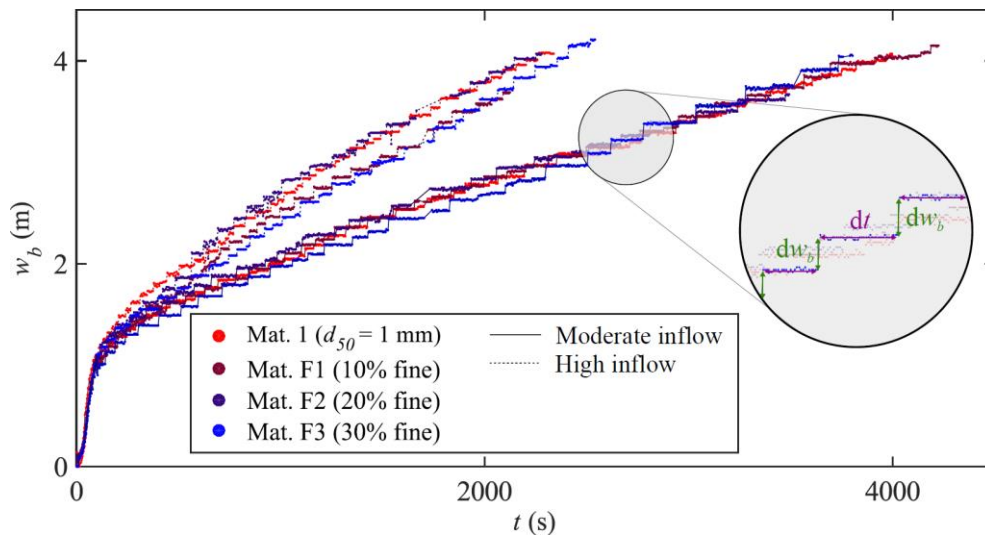


Figure 9 Evolution of breach width at crest level deduced from the high temporal resolution reconstructions of the breach profiles. The circled detail indicates how the failing lump widths  $dw_b$  and times between two lumps failure episodes  $dt$  are defined

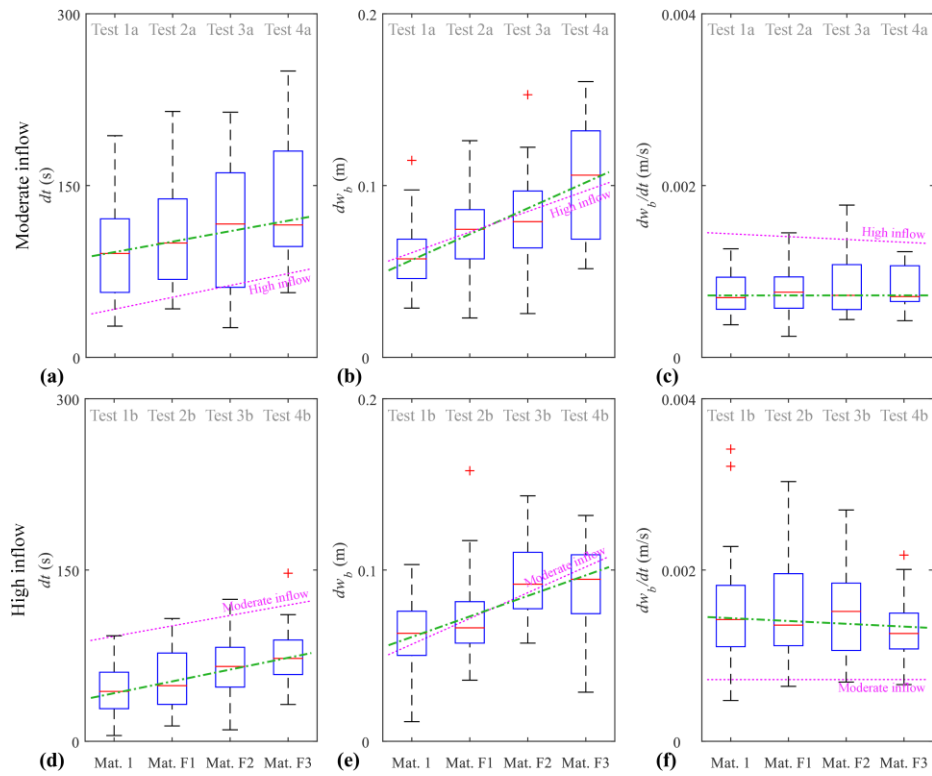


Figure 10 Whiskers plots of: (a) and (d) time  $dt$  between two successive slope failures, (b) and (e) width  $dw_b$  of failing lumps, and (c) and (f) breach widening speed during Stage 2. The red horizontal line is the median, and the box lower and upper limits correspond to the 25<sup>th</sup> and 75<sup>th</sup> percentiles, respectively. The whiskers extend to the most extreme data points not considered outliers and outliers are plotted individually using the red + symbol. The subplots (a) to (c) relate to tests with moderate inflow, (d) to (f) to tests with high inflow. The green and purple lines are linear regressions of the median  $dt$ ,  $dw_b$ , and  $dw_b/dt$  values for tests with different material compositions

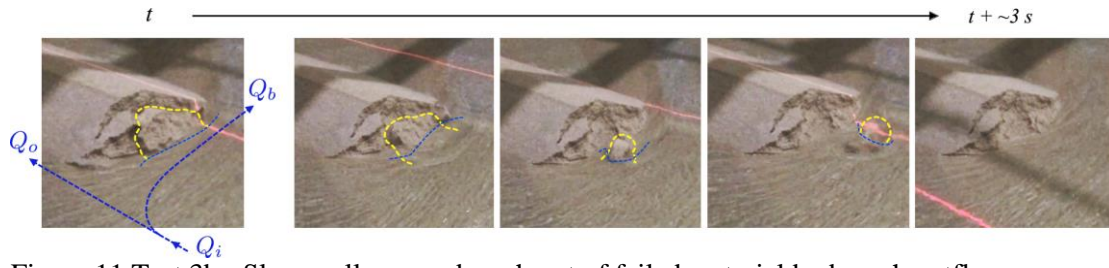


Figure 11 Test 3b - Slope collapse and wash out of failed material by breach outflow